Measurement of the helicity dependence for single π^0 photoproduction from the deuteron

F. Cividini,[1] M. Dieterle,[2] S. Abt,[2] P. Achenbach,[1] P. Adlarson,[1] F. Afzal,[3] Z. Ahmed,[4] J.R.M. Annand,[5] H.J. Arends,[1] M. Bashkanov,[6] R. Beck,[3] M. Biroth,[1] N. Borisov,[7] A. Braghieri,[8] W.J. Briscoe,[9] C. Collicott,[1] S. Costanza,[8,10] A. Denig,[1] A.S. Dolzhikov,[7] E.J. Downie,[9] P. Drexler,[1] S. Fegan,[6] A. Fix,[11] S. Gardner,[5] D. Ghosal,[2] D.I. Glazier,[5] I. Gorodnov,[7] W. Gradl,[1] M. Günther,[2] D. Gurevich,[12] L. Heijkenskjöld,[1] D. Hornidge,[13] G.M. Huber,[4] A. Käser,[2] V.L. Kashevarov,[1] S.J.D. Kay,[4] M. Korolija,[14] B. Krusche,[2] A. Lazarev,[7] K. Livingston,[5] S. Lutterer,[2] I.J.D. MacGregor,[5] D.M. Manley,[15] P.P. Martel,[1] R. Miskimen,[16] M. Mocanu,[6] E. Mornacchi,[1] C. Mullen,[5] A. Neganov,[7] A. Neiser,[1] M. Ostrick,[1] D. Paudyal,[4] P. Pedroni,[8,*] A. Powell,[5] T. Rostomyan,[2,†] V. Sokhoyan,[1] K. Spieker,[3] O. Steffen,[1] I. Strakovsky,[9] T. Strub,[2] A. Thiel,[3] M. Thiel,[1] A. Thomas,[1] Yu.A. Usov,[7] S. Wagner,[1] D.P. Watts,[6] D. Werthmüller,[6,‡] J. Wettig,[1] L. Witthauer,[2] M. Wolfes,[1] and N. Zachariou[6]

(The A2 Collaboration at MAMI)

[1]*Institut für Kernphysik, University of Mainz, D-55099 Mainz, Germany*
[2]*Departement Physik, Universität Basel, CH-4056 Basel, Switzerland*
[3]*Helmholtz-Institut für Strahlen- und Kernphysik, Universität Bonn, D-53115 Bonn, Germany*
[4]*University of Regina, Regina, Saskatchewan S4S 0A2, Canada*
[5]*SUPA School of Physics and Astronomy, University of Glasgow, Glasgow G12 8QQ, United Kingdom*
[6]*Department of Physics, University of York, Heslington, York, Y010 5DD, UK*
[7]*Joint Institute for Nuclear Research, 141980 Dubna, Russia*
[8]*INFN Sezione di Pavia, I-27100 Pavia, Italy*
[9]*The George Washington University, Washington, DC 20052-0001, USA*
[10]*Dipartimento di Fisica, Università di Pavia, Pavia; Italy*
[11]*Tomsk Polytechnic University, 634034 Tomsk, Russia*
[12]*Institute for Nuclear Research, 125047 Moscow, Russia*
[13]*Mount Allison University, Sackville, New Brunswick E4L 1E6, Canada*
[14]*Rudjer Boskovic Institute, HR-10000 Zagreb, Croatia*
[15]*Kent State University, Kent, Ohio 44242-0001, USA*
[16]*University of Massachusetts, Amherst, Massachusetts 01003, USA*

The helicity-dependent single π^0 photoproduction cross section on the deuteron and the angular dependence of the double polarisation observable E for the quasi-free single π^0 production off the proton and the neutron have been measured for the first time from the threshold region up to the photon energy 1.4 GeV. The experiment was performed at the tagged photon facility of the MAMI accelerator and used a circularly polarised photon beam and longitudinally polarised deuteron target. The reaction products were detected using the large acceptance Crystal Ball/TAPS calorimeter, which covered 97% of the full solid angle. Comparing the cross section from the deuteron with the sum of free nucleon cross sections provides a quantitative estimate of the effects of the nuclear medium on pion production. In contrast, comparison of E helicity asymmetry data from quasi-free protons off deuterium with data from a free proton target indicates that nuclear effects do not significantly affect this observable. As a consequence, it is deduced that the helicity asymmetry E on a free neutron can be reliably extracted from measurements on a deuteron in quasi-free kinematics.

I. INTRODUCTION

Despite many decades spent in intense research, many open questions remain regarding the the structure of the nucleon. The strong interaction plays a decisive role in the internal dynamics of the nucleon and its excited states, similarly to the way the electromagnetic interaction relates to the fundamental properties of atomic excitation spectra. Therefore, the study of the nucleon's spectrum is a crucial step towards understanding its structure.

The resonance widths are determined by the strong interaction and are of the order of hundreds of MeV, whereas their spacing is no more than a few tens of MeV, which leads to a very large amount of overlapping. To disentangle and access the individual states in the nucleon's spectrum, measurement of different polarisation observables is of crucial importance.

In general, there are 8 spin amplitudes that can be used to describe single meson photoproduction on a nucleon. Due to parity conservation, the number of independent amplitudes reduces to 4. Since any observable is a Hermitian form in the amplitudes, there are 16 linearly independent observables. They can be accessed using different combinations of polarisation of the photon beam, the target and recoil nucleon polarisation as, for instance, discussed in detail in Ref. [1].

According to different theoretical studies (see, for example, Refs. [2–5]), it is sufficient to measure a limited set (no less than 8) of properly chosen observables to unambiguously determine all four spin amplitudes for single pion photoproduction. Furthermore, since the electromagnetic interaction does not conserve isospin, it is necessary to use both proton and

* E-mail:paolo.pedroni@pv.infn.it
† Now at Paul Scherrer Institute (PSI), CH-5232 Villigen PSI, Switzerland.
‡ Now at Paul Scherrer Institute (PSI), CH-5232 Villigen PSI, Switzerland

neutron targets to be able to access the isospin decomposition of the amplitudes. In view of these reasons, the A2 Collaboration has been performing a series of experiments in order to measure different polarisation observables in the region up to a photon energy 1500 MeV, both on the proton and on the neutron.

In the present paper, we report new data for the angular dependence of the helicity asymmetry E for single π^0 production on the neutron that were collected using a polarised photon beam along with a polarised nucleon target. When the polarisation of the recoil nucleons is not measured, the corresponding general cross section reads:

$$\begin{aligned}\frac{d\sigma}{d\Omega} = \frac{d\sigma_0}{d\Omega}\Big\{1 - P_L^\gamma \Sigma\cos(2\phi) \\ + P_x^T\left[-P_L^\gamma H\sin(2\phi) + P_\odot^\gamma F\right] \\ + P_y^T\left(T - P_L^\gamma P\cos(2\phi)\right) \\ + P_z^T\left[P_L^\gamma G\sin(2\phi) - P_\odot^\gamma E\right]\Big\},\end{aligned} \tag{1}$$

where σ_0 is unpolarised cross section. The notations P_L^γ, $P_\odot^\gamma$, and P_i^T, $i = x,y,z$, stand for degree of the beam and target polarisations, and the observables $\mathscr{O} = \Sigma, H, F, \ldots$ are the polarisation asymmetries. P_L^γ ($P_\odot^\gamma$) refers to the linear (circular) polarisation of the photon beam and P_z^T to the longitudinal polarisation of the target, while ϕ is the angle between the linear photon polarisation plane and the reaction plane. The latter is spanned by the incident photon momentum and the momentum of the outgoing pion.

During the data taking, the photon beam was circularly polarised, the target was longitudinally polarised. With these experimental conditions, Eq. (1) is reduced to:

$$\frac{d\sigma^{\uparrow\downarrow/\uparrow\uparrow}}{d\Omega} = \frac{d\sigma_0}{d\Omega}\Big\{1 \pm P_z^T P_\odot^\gamma E\Big\}, \tag{2}$$

where the notation $\uparrow\uparrow$ ($\uparrow\downarrow$) indicates the relative parallel (antiparallel) photon-target polarisation direction. From Eq. (2) the double polarisation observable E can also be presented as:

$$\begin{aligned}E = \frac{d\sigma^{\uparrow\downarrow}/d\Omega - d\sigma^{\uparrow\uparrow}/d\Omega}{d\sigma^{\uparrow\downarrow}/d\Omega + d\sigma^{\uparrow\uparrow}/d\Omega} = \\ = \frac{N^{\uparrow\downarrow} - N^{\uparrow\uparrow}}{N^{\uparrow\downarrow} + N^{\uparrow\uparrow}} \cdot \frac{1}{P_z^T} \cdot \frac{1}{P_\odot^\gamma} \cdot \frac{1}{d},\end{aligned} \tag{3}$$

where $N^{\uparrow\downarrow(\uparrow\uparrow)}$ indicates the number of events with a parallel (antiparallel) helicity configuration, and d is the dilution factor giving the fraction of polarised nucleons inside the target.

In view of the impossibility of creating an appropriate free neutron target, one has to rely on light nuclei, such as ^{3}He or deuterium, as effective neutron targets. For the present experiment, a deuterated butanol target was chosen, due to the possibility to reach high degrees of polarisation (up to about 70%) with a fast build-up time ($\sim$ some hours) and high relaxation times (several hundred hours).

For an unambiguous extraction of the cross section on a single nucleon, reliable control of various nuclear effects is required. In order to minimize their influence one uses, as a rule, quasi-free kinematics. In addition, a robust theoretical model that takes into account the most important nuclear effects, such as Fermi motion, admixture of the tensor forces, the Pauli exclusion principle and final state interactions, is also of vital importance. For this study, different additional reaction channels need to be measured in order to obtain an experimental quantitative evaluation of all of these effects.

In recent years, some of these issues have already been addressed with theoretical and experimental studies of other observables. The GWU-ITEP theoretical group has shown [6–9] that the maximum effect of final-state interactions (FSI), the main effect given by the nuclear environment, on particles from single pion photoproduction on the deuteron, is about 20% for the unpolarised cross section, while it is much smaller and consistent with experimental uncertainties for the different polarisation asymmetries observables.

In particular, the model described in Ref. [8] was used to extract the unpolarised differential cross section for the $\gamma n \to n\pi^0$ reaction from our previous measurement on a deuteron target [10] in the photon energy range $200 - 813$ MeV. Above 300 MeV, a satisfactory agreement was found between the extracted data and the SAID-MA19 partial wave analysis.

On the other hand, our recent data for the photon beam asymmetry of the π^0 production off neutrons bound in deuterons from 390 to 610 MeV [11] are well reproduced by the existing partial wave analyses for the lowest measured region while discrepancies appear only at the highest energies. This feature seems to indicate that nuclear effects have a smaller effect on polarization asymmetries since these observables measure ratios of absolute cross sections.

It is interesting to note that similar conclusions have been drawn from our previous studies on the beam-helicity asymmetry of both $\eta\pi$ and $\pi^0\pi^\pm$ pairs off protons and deuterons [12, 13]. In these cases, measured unpolarised absolute cross sections are reduced for the reactions on quasi-free protons on the deuteron with respect to the free proton data while the measured asymmetries do not show significant differences between these two cases. Moreover, also the measured beam-helicity asymmetry of $\eta\pi^0$ pair on C, Al and Pb [14] has been found to be not much affected by nuclear effects.

The main goal of the present work, which extends these studies to helicity-dependent observables, is then twofold: (i) to measure the helicity-dependent semi-inclusive cross section for single π^0 production on the deuteron to clearly evidence the role of the nuclear effects and (ii) to measure the E observable for single π^0 production on quasi-free neutrons and protons. In the latter case, the comparison with the data on a free proton allows to cross check and understand the influence of the nuclear environment on the single nucleon process. These new results extend the set of the angle-integrated E data that have already been published in Ref. [15].

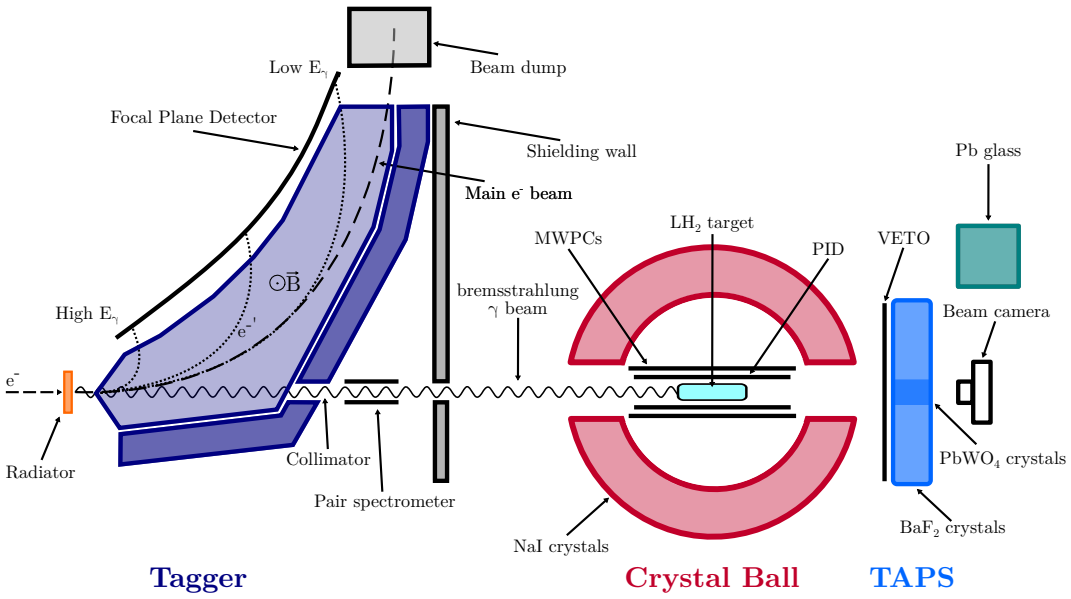

FIG. 1: A2 experimental setup with the photon tagging apparatus and detectors [16].

II. EXPERIMENTAL SETUP

The helicity-dependent data were measured during different beam time periods at the MAMI electron accelerator facility in Mainz, Germany [17]. Figure 1 shows a general sketch of the A2 experimental setup used for the measurement. Since this apparatus has been already previously described in detail (see, for instance, Refs. [15, 18, 19] and references therein), only the main characteristics relevant for the present measurement will be given here.

The photon beam is produced via bremsstrahlung when the primary polarised electron beam hits a thin amorphous radiator. To avoid polarisation-dependent photon flux values, the beam helicity was routinely flipped at a rate of 1 Hz.

The electron polarisation P_e was regularly determined with Mott scattering close to the electron source and found to be around 80% for all the different measurements. In addition, Moeller scattering at the radiator site was used as an additional polarisation monitor. A magnetic field applied after the radiator deflects the post-bremsstrahlung electrons in the focal plane and they are tagged by the Glasgow-Mainz spectrometer with an energy resolution of $\sim 2-5$ MeV, which corresponds to the width of the focal plane counters [20]. The photon beam passes through a 2 mm diameter collimator, reaching the target and detection apparatus. The degree of energy dependent circular photon polarisation was determined using the Olsen and Maximon formula [21], while the photon tagging efficiency (approximately 35%) has been measured once a day using a Pb-Glass Cerenkov detector in dedicated low flux runs. During the standard data taking operation, the fluctuations of the photon flux are monitored using a low-efficiency pair spectrometer located in the photon beamline after the collimator. From the comparison of the data from these detectors, an absolute systematic uncertainty of 4% has been estimated on the photon flux.

The target used for this experiment is the Mainz-Dubna Frozen Spin Target (FST) filled with deuterated butanol (C_4D_9OD) [22, 23]. The filling factor for the ~ 2 mm diameter butanol spheres into the 2 cm long, 2 cm diameter target container was estimated to be 60%, with a systematic uncertainty of 2% [22]. The target material is polarised using the Dynamic Nuclear Polarisation (DNP) effect [24], which required a magnetic field of 1.5 T and a temperature of $\sim$25 mK. Such conditions, in combination with a small holding magnetic field of 0.6 T which replaced the polarising magnet during the data taking phase, allowed regular relaxation times longer than $>$1000 h to be obtained. The target polarisation was measured with an NMR system before and after the data taking period and then interpolated exponentially at intermediate times.

To enhance the efficiency of the DNP procedure, the butanol was chemically doped with highly polarisable paramagnetic centers. In the first two beam times, the trityl radical Finland D36 was used, with typical polarisation degrees of about 60%. However, for these runs there was a problem in the absolute determination of the polarisation, caused by small field inhomogeneities (B $\leq$ 1.78 mT) of the polarising magnet. An additional third beam time, comprising about 30% of the total collected statistics, used a different radical (Tempo), which results in lower polarisation degrees (about 30%), but is not sensitive to small field inhomogeneities. The absolute scale of all helicity-dependent cross sections and asymmetries were renormalized to this additional beam time and cross checked with a parallel analysis on η photoproduction [18].

From these analyses, similar to those in Ref. [15], a conservative relative systematic error of 10% has been estimated for the degree of target polarisation.

For the evaluation of the denominator of Eq. (3), it is also

crucial to study the contribution of the unpolarised C and O nuclei inside the target material. Some dedicated data takings with a carbon target were performed for this purpose. This target was made from a foam with the same density and the same geometry as the butanol target.

Photons from π^0 decay and recoil nucleons were detected by the Crystal Ball-TAPS apparatus. The Crystal Ball (CB) is located around the target cell and covers the full azimuthal (ϕ) angle and polar (θ) from 21° to 159° [25]. It is made of 672 NaI(Tl) crystals covering a large solid angle and has a very high detection efficiency for photons. Inside the CB there are two Multi-Wire Proportional Chambers (MWPCs) and a Particle Identification Detector (PID), made of a barrel of 24 plastic scintillators. The combination of all these detectors allows for a precise tracking and identification of charged particles. TAPS is a hexagonal wall covering the polar forward region outside the CB acceptance and it is made of 366 BaF_2 and 72 $PbWO_4$ crystals [26, 27]. In front of the TAPS array a 5 mm thick plastic scintillator wall (VETO) is used for charged particles identification. The combination of the large acceptance CB and TAPS covers $\sim$ 97% of the solid angle, allowing precise measurements to be made of both the energy and the angles of the photoemitted particles.

III. DATA ANALYSIS

After the energy and time calibration of all detector modules, the data from the butanol target were analysed together with data from the carbon foam. All different algorithms have been tested and checked, both with simulated and real data to obtain an optimal rejection of the background coming from the unpolarised target nucleons.

Detailed descriptions of the different analysis algorithms have been given before (see, for instance Refs. [15, 18, 19] and references therein). Therefore, only a summary of the main analysis steps needed for the identification of the measured observables on the π^0 production on deuterium will be given here.

The π^0 identification algorithm is common to all the performed analyses, while the methods for both the nucleon identification and the subtraction of the unpolarised background were only used for the evaluation of the E observable.

The detector response and the absolute efficiency of the detection and reconstruction of the single π^0 photoproduction channel, needed for the determination of the absolute cross section, were evaluated using a GEANT4 based simulation [28] which models accurately the geometry and composition of the detector setup and accounts for electronic thresholds.

The candidate events accepted for all analyses were those with 2 or 3 clusters of energy deposition reconstructed inside of the detection apparatus.

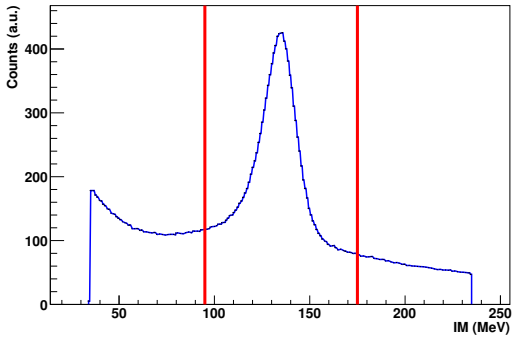

FIG. 2: Two photon invariant mass (IM) distribution from the π^0 reconstruction procedure for all the candidate events. The red lines define the $\pm$ 40 MeV cut (corresponding to an experimental resolution of about 2.5 σ) around the nominal m_{π^0} value.

A. π^0 reconstruction and identification

The first offline analysis step was the evaluation of the two photon invariant mass (IM) using all the neutral clusters of the event. For all events with more than 2 neutral hits, all possible combinations were used to calculate the two photon invariant mass and only the combination giving the closest value to the nominal π^0 mass was retained for successive analysis steps.

If the calculated IM value is included in a window of $\pm$40 MeV, around the PDG π^0 nominal mass, which corresponds to an experimental resolution of about 2.5 σ, the event has been selected for the next step. In Fig. 2, the overall IM distribution is shown with the applied cut region.

For events with more than two neutral hits, where ambiguities between photons and neutrons can occur, an additional test was performed by comparing the invariant mass of the two photon candidate $m_{\gamma_1\gamma_2}$ to the nominal π^0 mass m_{π^0} as:

$$\chi^2_{\pi^0} = \left(\frac{m_{\gamma_1\gamma_2} - m_{\pi^0}}{\Delta m_{\gamma_1\gamma_2}} \right)^2 , \qquad (4)$$

where $\Delta m_{\gamma_1\gamma_2}$ is given by the simulated detector response. The two neutral clusters from the combination with the lowest $\chi^2_{\pi^0}$ value was selected as π^0 decay photons and the remaining neutral hit as a neutron candidate. As previously shown (see Refs. [15, 29] and references therein), this method has proven to be very effective in resolving ambiguities in neutron-photon separation in the $n\pi^0(\pi^0)$ final states.

Only events with a reconstructed π^0 and with an IM value within the selected window were accepted for the subsequent analysis stages.

The following step was the evaluation of the event missing mass (MM), where the recoil nucleon of the reaction $\gamma N \rightarrow \pi^0 N$ was considered as a missing particle, even when it had been detected. This parameter has been calculated as follows:

$$\mathrm{MM} = \sqrt{(E_\gamma + m_N - E_{\pi^0})^2 - (\overrightarrow{p}_\gamma - \overrightarrow{p}_{\pi^0})^2} , \qquad (5)$$

where E_γ and p_γ are the laboratory energy and momentum of the incoming photon, m_N is the nucleon mass in the initial state, E_{π^0} and p_{π^0} are the reconstructed π^0 total energy and momentum.

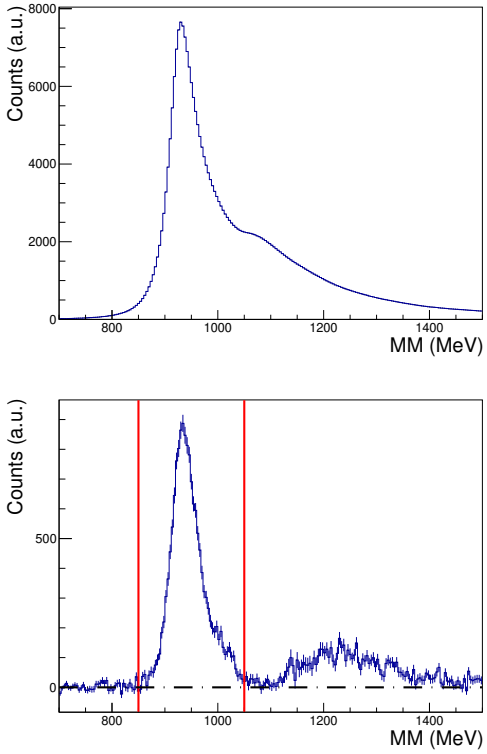

FIG. 3: Missing mass (MM) distribution for the sum (top) and the difference (bottom) of the MM distributions of the parallel and anti-parallel event configurations. The acceptance event region is inside the red vertical lines at MM = 850 and 1050 MeV.

The obtained MM distribution which, in comparison to the free-nucleon case is broadened due to the Fermi motion of the initial-state nucleon, is shown in the top part of Fig. 3. As seen in this figure, a consistent background was still present, in particular in the right tail of the distribution. This is mainly due to unpolarised carbon and oxygen nuclei in the butanol molecules. In the bottom part of Fig. 3, the difference between the missing mass distributions of the parallel and anti-parallel event configurations is shown. This allows a verification of the previous hypothesis since, in this case, the background from unpolarised nuclei cancels. As expected, the tails are now vanishing at both ends and the distribution is centered at the nominal value of the nucleon mass.

Only the events with a MM value within 850 and 1050 MeV (the region between the vertical lines of Fig. 3) have been taken into account for the following steps of the analysis. This cut also eliminates the additional background showing up on the right tail of the MM distribution, that comes from the $\pi^0\pi^0$ and $\pi^0\pi^\pm$ processes when the additional photoproduced pion had, at least partially, escaped the detection inside our apparatus.

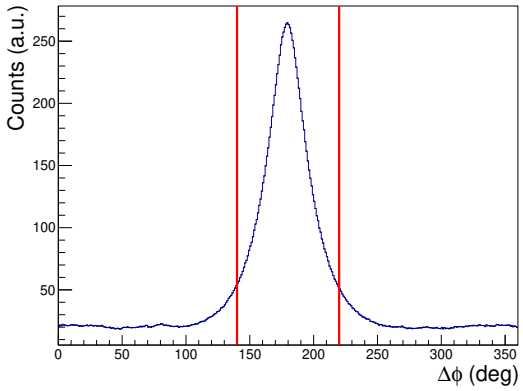

FIG. 4: Distribution, of the $\Delta\phi$ azimuthal angle between the reconstructed π^0 and the nucleon track candidate for all events accepted by the MM cut. The acceptance event region is inside the red vertical lines at $\Delta\phi = 140^\circ$ and 220°.

B. Proton and neutron identification

For the evaluation of the E asymmetry for the single π^0 on quasi-free protons and neutrons, only the events having one additional track not used for the π^0 reconstruction have been selected from the previously obtained sample.

In the first step of this analysis, the coplanarity between the reconstructed π^0 and the additional track has been checked, since, when the Fermi momentum of the target nucleon is neglected, the incident photon, the π^0 and the recoil nucleon lie in the same plane, due to momentum conservation. Simulations show that the effect due to the Fermi momentum of the target nucleon does not change the peak position, but only slightly enlarges the width of the distribution.

The mean value of the difference $\Delta\phi$ between the azimuthal angles of the π^0 and the recoil nucleon must therefore be 180°, as seen from the obtained $\Delta\phi$ distribution presented in Fig. 4 for all event with a reconstructed π^0 and a candidate nucleon track. Events having this additional track not co-planar with the identified π^0, i.e. when $\Delta\phi$ was outside the acceptance region defined in the previous figure, were removed from the analysis. Tracks satisfying both this and the MM condition are considered to be proton or neutron candidates depending on whether the track is charged or neutral, that is with or without a hit either in the PID or in the VETO detector.

Thereafter additional conditions, discussed below, are applied to identify participating nucleons.

In the forward region covered by TAPS, it is possible to perform a Pulse Shape Analysis (PSA) [15], thanks to the two ("fast" and "slow") components of the signals from the BaF_2 crystals. These components were integrated over two different ranges (short gate: 40 ns; long gate: 2 μs) to respectively obtain the E_s and E_l energy components. For light particles, such as photons, the two components are quite similar, while, for massive particles E_s is smaller than E_l. To better highlight this difference, it is convenient to use the transformation to the

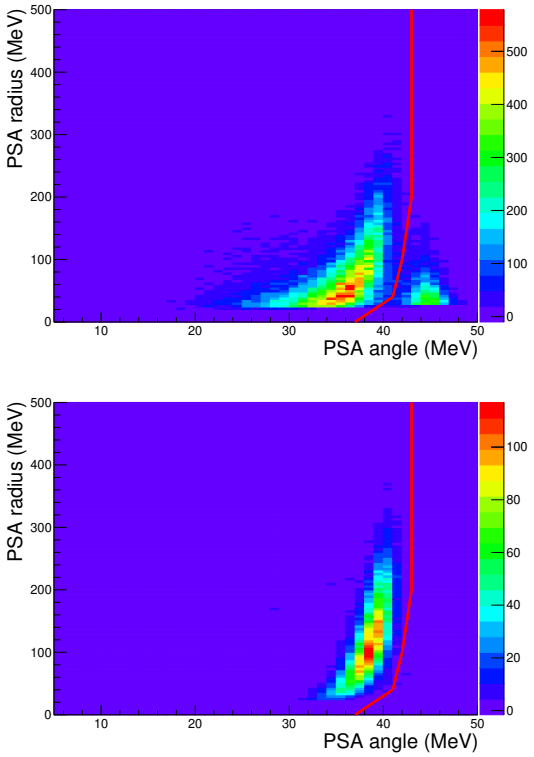

FIG. 5: PSA plots for neutral (top) and charged (bottom) tracks after π^0 reconstruction, MM and coplanarity cuts. The neutron and proton candidates lying on the right of the red lines have been rejected.

PSA radius r_{PSA} and angle ϕ_{PSA}, which are defined as:

$$r_{PSA} = \sqrt{E_s^2 + E_l^2} \quad ; \quad \phi_{PSA} = \arctan E_s/E_l \ . \qquad (6)$$

Since, for photons $E_s \approxeq E_l$, while, for massive particles $E_s < E_l$, photons are evident at $\phi_{PSA} \approxeq 45°$, independently of r_{PSA}, while neutrons are located at smaller angles.

In Fig. 5, the obtained PSA spectra for the proton and neutron candidates are given. Events with particle candidates on the right of the red curve have been rejected. In the charged track case, no relevant background was present even before this cut was applied.

Due to the good time resolution of the TAPS detector and the relatively long distance between the target and the detector (about 1.5 m), a time-of-flight (ToF) analysis was also performed, to refine both the neutron and the proton selection.

In this case, photon candidates form a band at a constant ToF corresponding to the target - detector, distance while non-relativistic protons and neutrons lie in a band at higher ToF values.

The results of this analysis are shown in Fig. 6, where the ToF (expressed as difference with the event trigger time) of both for the accepted neutron (top plot) and proton (bottom plot) candidates after the PSA cut is compared to the total deposited particle energy.

Guided by the simulation, a residual background was rejected by the horizontal red lines shown in Fig. 6.

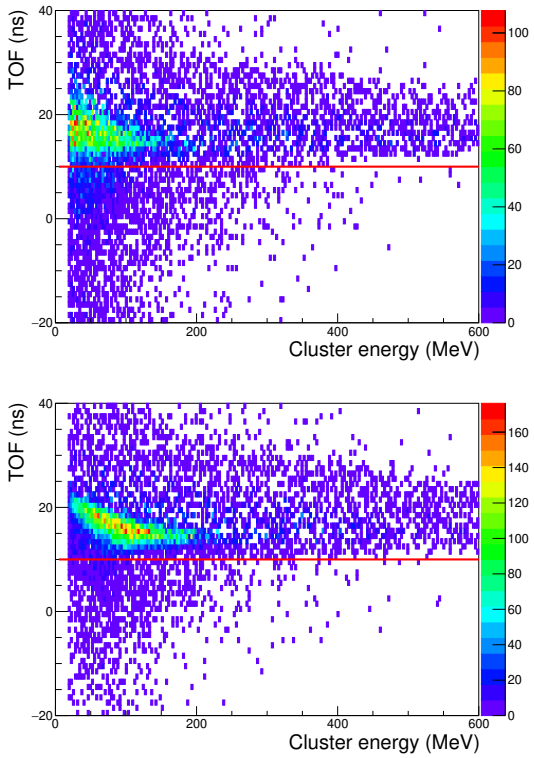

FIG. 6: ToF analysis for neutral (top) and charged (bottom) tracks after the PSA cut. The neutron and proton candidates lying below the red lines have been rejected.

For neutral particles detected in the CB, a cluster size analysis was used to cross check the neutron selection performed with the $\chi^2_{\pi^0}$ selection method previously described (see Eq. 4).

As shown by a simulation of the quasi-free $n\pi^0$ process, neutron clusters consist of very few detector elements (just one in many cases), while high energy photons coming from the π^0 decay produce, on average, larger clusters due to the much larger amount of deposited energy.

In Fig. 7, the experimental cluster size distribution is compared to the deposited energy in CB for photons coming from the π^0 decay, selected from events with two neutral clusters and a reconstructed π^0 (top plot), and for the third cluster, not selected as part of a π^0 decay, in events with 3 neutral clusters (bottom plot). Neutrons from the $n\pi^0$ channel congregate in the bottom-left part of the plot, while photons mainly populate the mid and top-left parts. Guided by the quasi-free $n\pi^0$ simulation, a final selection cut, shown by the red line in the bottom plot of Fig. 7, was applied so that no significant background is left after the end of the neutron selection procedure.

As a final cross check of the proton selection analysis, the $\Delta E - E$ plots both for tracks detected in CB (using PID and CB energy information) and TAPS (using VETO and TAPS energy information) were constructed. Figure 8 shows the $\Delta E - E$ plot obtained with the PID-CB and the VETO-TAPS

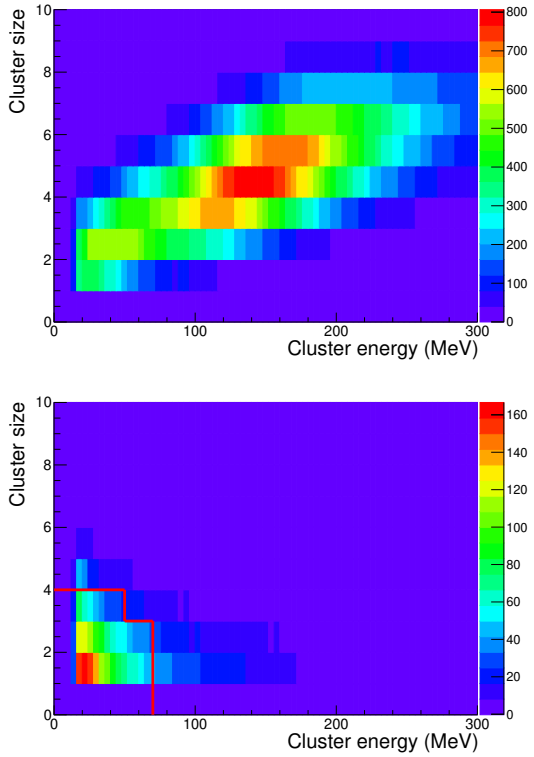

FIG. 7: Cluster size distribution versus the energy released in CB for all tracks of events with 2 neutral clusters and a reconstructed π^0 (top plot) and for the unapaired clusters in events with 3 neutral clusters and a reconstructed π^0 (bottom plot). The tracks lying below the red line were considered as neutrons.

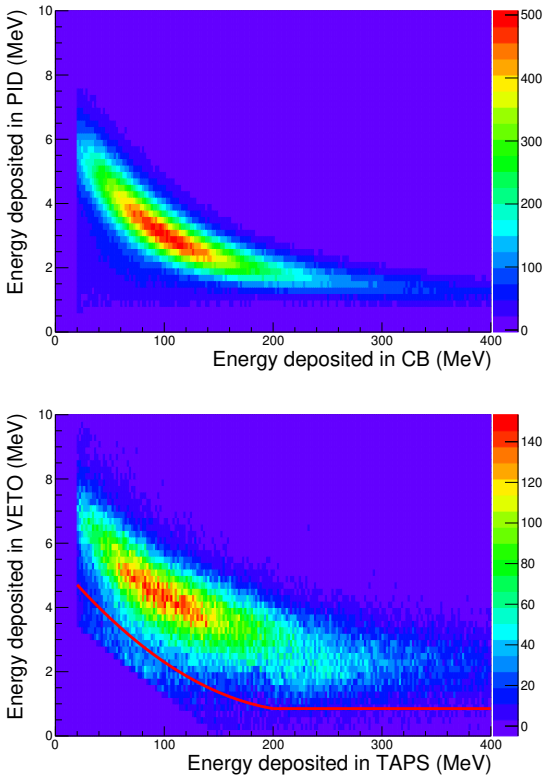

FIG. 8: $\Delta E - E$ plot with the energy information from PID and CB (top plot) and VETO and TAPS (bottom plot) after coplanarity and MM cuts. In the bottom plot, tracks lying above the red line were considered as protons.

detectors, respectively. In both cases, the proton band is very clean, which proves the validity of the selection procedure. For the VETO-TAPS combination, a final selection cut, shown by the red line in the bottom plot of Fig. 8, was applied to suppress a small residual background.

C. Unpolarised background subtraction

In the extraction of the E observable, the evaluation of the background coming from unpolarised C and O target nuclei is crucial for the correct evaluation of the denominator of Eq. 3. As previously mentioned, dedicated data were taken with a carbon foam target to separately measure this background contribution, under the assumption that the nucleons bound in C and O nuclei give the same response to the incoming photons.

Due to this effect, Eq. 3 has to be modified as:

$$E_p(W,\theta) = \frac{1}{P_z^T} \cdot \frac{1}{P_\odot^\gamma} \times \frac{N_{\mathrm{BUT}}^{\uparrow\downarrow}(W,\theta) - N_{\mathrm{BUT}}^{\uparrow\uparrow}(W,\theta)}{(N_{\mathrm{BUT}}^{\uparrow\downarrow}(W,\theta) + N_{\mathrm{BUT}}^{\uparrow\uparrow}(W,\theta)) - s \cdot N_C(W,\theta)}, \quad (7)$$

where W in the total center-of-mass energy and the subscripts "BUT" and "C" indicate the data from butanol and carbon targets, respectively, and s is the scaling factor needed to normalize the different data sets available.

The scaling factor s was determined using different methods: i) absolute normalisation by photon flux, target density and detection efficiency; ii) using MM or coplanarity spectra in a region where the quasi-free nucleons do not contribute (MM $\sim$ 1050 MeV).

A typical example of the obtained MM spectra is shown in Fig. 9 for events with quasi-free protons. The s factor was used to scale the original carbon distribution (magenta dots in Fig. 9) and the MM distribution from quasi-free protons bound inside the deuteron (green dots) was evaluated by subtracting the scaled carbon distribution (red dots) from the one from deuterated butanol (blue dots). The subtracted distribution is in very good agreement with the simulated quasi-free proton distribution (black dots) for MM values below 1050

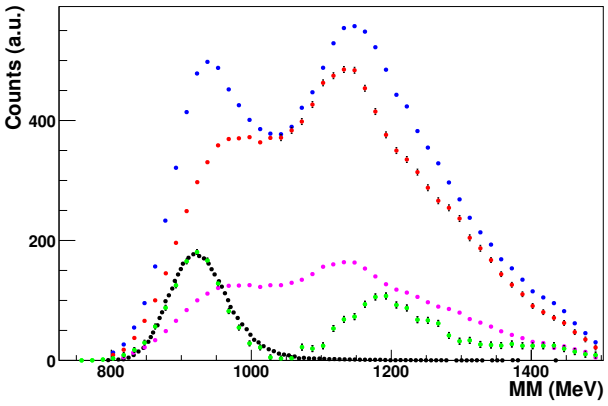

FIG. 9: Subtraction of the carbon background for proton events using the missing mass plots obtained from D-butanol and carbon data for W (total center-of-mass energy) between 1450 and 1480 MeV. The different points represent the missing mass distribution for: the D-butanol target (blue dots), the carbon target (magenta dots), the scaled carbon (red dots) and the proton events (green dots) obtained by subtracting the scaled carbon events from the D-butanol events. The black dots show the simulated distribution of quasi-free proton events from a deuterium target.

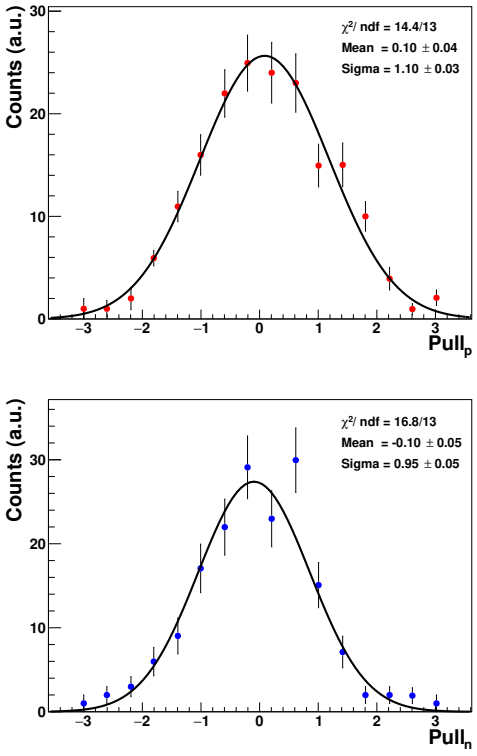

FIG. 10: Distribution of the Pull variable (Eq. (8)) for protons (top) and neutrons (bottom).

MeV. As in Fig. 3, it also shows the good rejection of events from double pion reactions achieved with the MM cut. In general, the more pronounced unpolarised contributions were found at the highest photon energy values and in the most extreme angular regions.

All the applied methods gave quite similar and statistically equivalent results. As an example, in Fig. 10 the distribution of the Pull variable:

$$Pull_{p(n)} = \frac{(E_1 p(n) - E_2 p(n))}{\sqrt{\sigma^2_{1p(n)} + \sigma^2_{2p(n)}}} \tag{8}$$

is shown, where $E_1 p(n)$ and $E_2 p(n)$ are the asymmetries evaluated at each θ and W value using the two methods described above on different data subsets for the proton (neutron) case. The solid lines represent the best-fit gaussians obtained from the data, whose parameters are given in the legends. According to expectations, both the mean and the variance resulting from the fit are compatible with the standard gaussian parameters. The final E central values are taken as the weighted average between the different procedures [30, 31].

The differences in the E values obtained with these methods were used to evaluate the systematic uncertainties associated to this procedure. In most of the measured energy and angular bins, the relative values of these uncertainties were estimated to be in the range of $[2\% - 10\%]$, with the exception of the most forward angular bin, where the limited statistics due to the low detector efficiency often causes larger uncertainties.

This procedure was performed independently for proton and neutron events, with different scaling factors obtained for each W bin when method ii) was applied. The angular dependence of the scaling factors was also checked, but found to be negligible.

D. Inclusive single π^0 photoproduction on the deuteron: $\gamma d \to \pi^0 B$ ($B = pn$ or d)

The helicity-dependent cross section difference $(d\Delta\sigma/d\Omega)$ for single π^0 on the deuteron can be expressed as follows (see also Eq. 3) :

$$\frac{d\Delta\sigma}{d\Omega}(E_\gamma) = \frac{d\sigma^{\uparrow\uparrow}}{d\Omega}(E_\gamma) - \frac{d\sigma^{\uparrow\downarrow}}{d\Omega}(E_\gamma) = \tag{9}$$
$$= 2 \cdot \frac{N^{\uparrow\uparrow}(E_\gamma,\theta) - N^{\uparrow\downarrow}(E_\gamma,\theta)}{I_\gamma(E_\gamma)\cdot\varepsilon_{DET}(E_\gamma,\theta)\cdot\Delta\Omega\cdot n} \cdot \frac{1}{P_\odot^\gamma} \cdot \frac{1}{P_z^T},$$

where I_γ is the total photon flux, with $I_\gamma = 2I_\gamma^{\uparrow\uparrow} = 2I_\gamma^{\uparrow\downarrow}$, due to our experimental conditions (see Sect. II), ε_{DET} is the detector global π^0 detection efficiency, $\Delta\Omega$ is the solid angle factor and n is the surface density of polarised deuterons. For this observable, it was necessary to select all events with a π^0 reconstructed in the CB-TAPS setup, without additional requirements. The relative systematic uncertainty of ε_{DET}, estimated to be 4%, was evaluated by examining the cross section variations due to the different cuts and selection conditions applied both to the experimental and the simulated data. The values of the helicity-dependent total cross section difference $\Delta\sigma$ are obtained by integrating Eq. (9) over the full solid angle. In

this case, no unpolarised contribution needs to be evaluated since the effect of the unpolarised C and O nuclei in the target vanish in the difference.

E. E asymmetry for single π^0 on quasi-free protons and neutrons

In addition to the detection of one π^0, the events selected during the analysis were required to also have a proton or neutron identified. A good quality of the nucleon selection from any polarised and unpolarised background is crucial for a highly precise calculation of the E observable. This goal has been achieved by the selection previously described.

F. Systematic uncertainties

The different sources of systematic uncertainties previously discussed are summarized in Tab. I.

Sources of common global systematic uncertainties come from the absolute photon flux normalization, particle reconstruction efficiency (these contributions are only relevant for the cross section evaluation), from the beam and target polarisation values and from the target surface density.

The point-to-point systematic error contribution from the unpolarised background subtraction is only relevant for the E observable and it is dependent on the analysed W and $\cos(\theta_{\pi^0}^{\mathrm{CM}})$ bins, as described in Section III C.

TABLE I: Systematic uncertainties of the present data analysis.

Target polarisation	$\pm 10\%$
Unpolarised background subtraction	$\pm 2-10\%$
Tagging efficiency	$\pm 4\%$
Dtector efficiency	$\pm 4\%$
Beam polarisation	$\pm 3\%$
Target filling factor	$\pm 2\%$

IV. RESULTS

A. Inclusive single π^0 photoproduction cross section on the deuteron

The total helicity-dependent section difference $\Delta\sigma$ for the $\gamma d \to \pi^0 B\,(B = pn \,\mathrm{or}\, d)$ reaction, is shown in Fig. 11a) (black points) in the region from E_γ=160 MeV up to 1390 MeV. It is compared to the data (red points) previously published by the GDH collaboration [32]. With respect to the previous results, this work provides new data covering a wider energy range with better statistics.

In Fig. 11b), only the results for $E_\gamma > 550$ MeV are plotted to better highlight the high-energy behaviour. The different solid lines show the predictions for the elementary (proton+neutron) cross sections given by different multipole analyses: SAID-MA19 [10] (blue line); BnGa-2019 [33] (green line); MAID-2021 [34] (red line).

The major part of discrepancy between the experimental results and the calculation is primarily due to different nuclear effects, in particular final state interactions (FSI), which are especially important in the $\Delta(1232)$ resonance region. The dashed red line shows the theoretical results given by the deuteron calculation performed by A.Fix. This prediction is based on the model of Refs. [35, 36], in which the elementary MAID-2021 amplitudes for the $\gamma N \to \pi^0 N$ are embedded instead of the MAID-2003 version used in [36].

In the insert histogram of Fig. 11a) the predictions of the coherent ($\gamma d \to \pi^0 d$) and incoherent ($\gamma d \to \pi^0 pn$) cross sections are also presented separately. It can be seen that the coherent process gives a sizeable contribution to the π^0 production process only at photon energies below 400 MeV. As seen in Fig. 11, after the nuclear effects are included, the calculated cross section difference $\Delta\sigma$ visibly decreases. The major source of this reduction, as discussed in Ref.[36], is the interaction between the final nucleons in the $^3S_1$ state. In contrast to the charged channels, $\gamma d \to \pi^+ nn$ and $\gamma d \to \pi^- pp$, the plane wave cross section for $\gamma d \to \pi^0 np$ effectively contains a spurious contribution of the coherent channel $\gamma d \to \pi^0 d$. The latter is due to the trivial fact that the final NN plane wave is not orthogonal to the deuteron ground state. After this spurious contribution is projected out, the resulting interaction effect turns out to be of the same order as for charged pion production, about 2 %. Inclusion of the πN rescattering leads to further reduction of the cross section.

Thus, the total FSI effect in the Δ region is a decrease of the total cross section difference $\Delta\sigma$ by about 20 % in both helicity states. At the same time, as evident from Fig. 11, this reduction is not sufficiently strong to reproduce the experimental data. The source of the remaining deviation is still unclear. In particular, as shown in Ref. [36], the multiple scattering corrections in the πNN system are insignificant, and their inclusion cannot explain the discrepancy.

In Fig. 11b), as in the free-nucleon case, a dip in the experimental $\Delta\sigma_{\pi^0}$ values can be observed near the η production threshold due to the intereference between $N\pi^0$ and $N\eta$ channels, while, for E_γ values just above $\approx$ 1 GeV, also the effects due to the excitation of the $F_{15}(1680)$ resonance are reduced with respect to the free-nucleon case.

The differential cross section difference $d\Delta\sigma/d\Omega$ results for individual photon energy bins from 162 to 1387 MeV are shown in Figs. 12 and 13, respectively. No previous data for this observable have previously been reported. As before, our data are compared to the free (proton+neutron) cross section from SAID-MA19, BnGa-2019, MAID-2021 multipole analyses and to the calculation on the deuteron.

The overall trend of the data is fairly well reproduced by all models. From the comparison between the free nucleon and the deuteron results, it can be noticed that, in general, nuclear effects are quite important for all angles over most of the energy range covered by the present measurements. They also are more relevant at the lowest $\theta_{\pi^0}^{\mathrm{lab}}$ values, as predicted in Ref. [8] for the unpolarised differential cross section and,

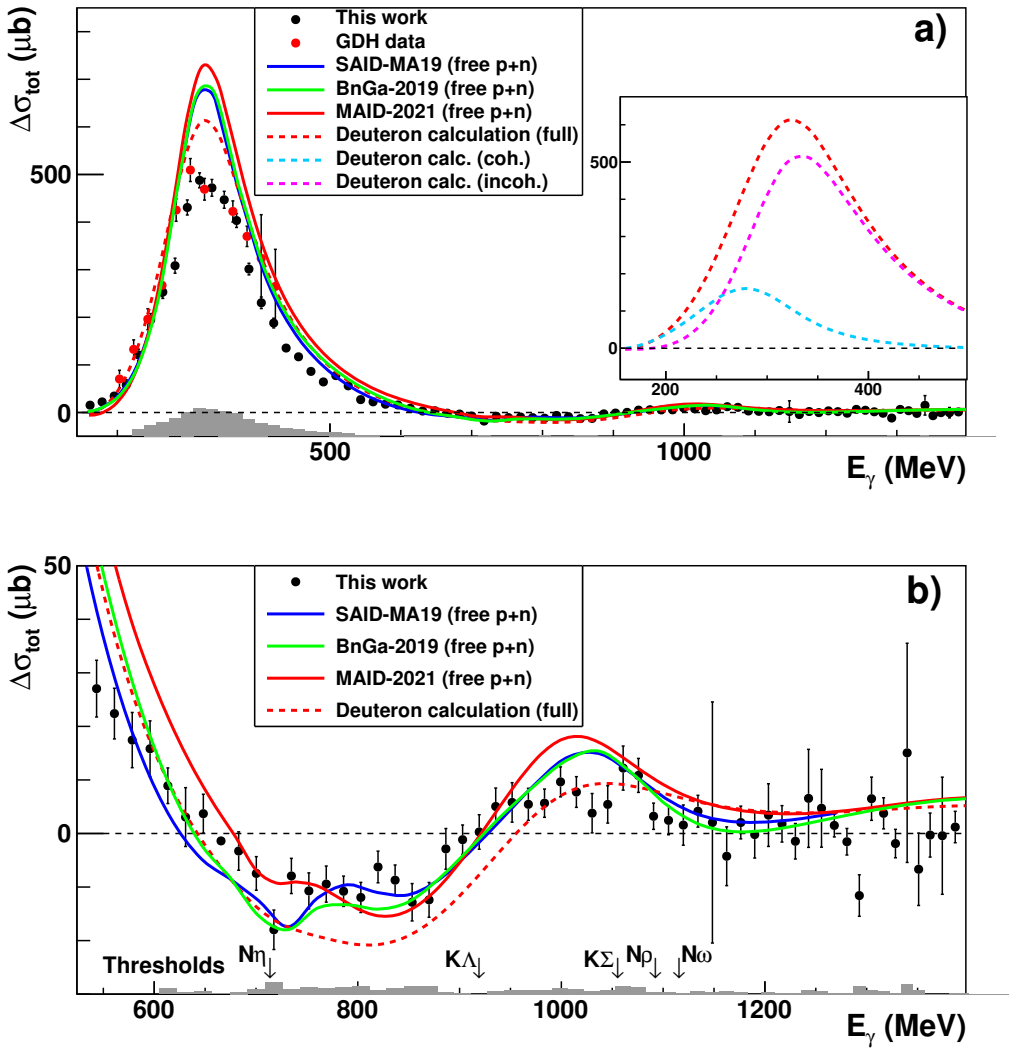

FIG. 11: Inclusive polarised π^0 photoproduction cross section on the deuteron ($\gamma d \to \pi^0 B$). The new results (black points) are compared with the results from the GDH Collaboration (red points)[32]. The different solid lines show the predictions for the free (proton+neutron) sum of different analyses. Blue line: SAID-MA19 [10] ; green line: BnGa-2019 [33]; red line: MAID-2021 [34]. The dashed line shows the predictions for $\gamma d \to \pi^0 B$ ($B = pn$ or d) obtained using the model of Refs. [35, 36] with the new MAID-2021 amplitudes for $\gamma N \to \pi N$. The insert shows separate contributions from the incoherent $\gamma d \to \pi^0 pn$ and the coherent $\gamma d \to \pi^0 d$ channels. In (b) the markers at the energies corresponding to opening of other channels are also indicated. The contributions of all the systematic uncertainties (see Sect. III F) are depicted as grey bars.

apart from the first few energy intervals, they lead to a visible decrease in the absolute value of the cross section.

B. Double polarisation E observable for single π^0 on quasi-free proton

The results for the double polarisation observable E on quasi-free protons are presented in Figs. 14 and 15, where they are compared to the free proton results reported by CBELSA/TAPS collaboration [37, 38] when the difference between the measured central W bin values is less than 8 MeV.

The different solid lines represent free proton predictions from SAID-MA19 (blue curves), BnGa-2019 (green curves) and MAID-2021 (red curves) multipole analyses which are constrained by the CBELSA/TAPS data.

The dashed red lines are predictions of the model of Refs. [35, 36], where the most important nuclear effects, such as Fermi motion, presence of the D-state in the deuteron wave function, Pauli exclusion principle, and first-order rescattering of the final particles, are taken into account.

The results obtained for the free and the quasi-free proton targets are rather close to each other and agree within statistical and systematic uncertainties. This is an indication that the

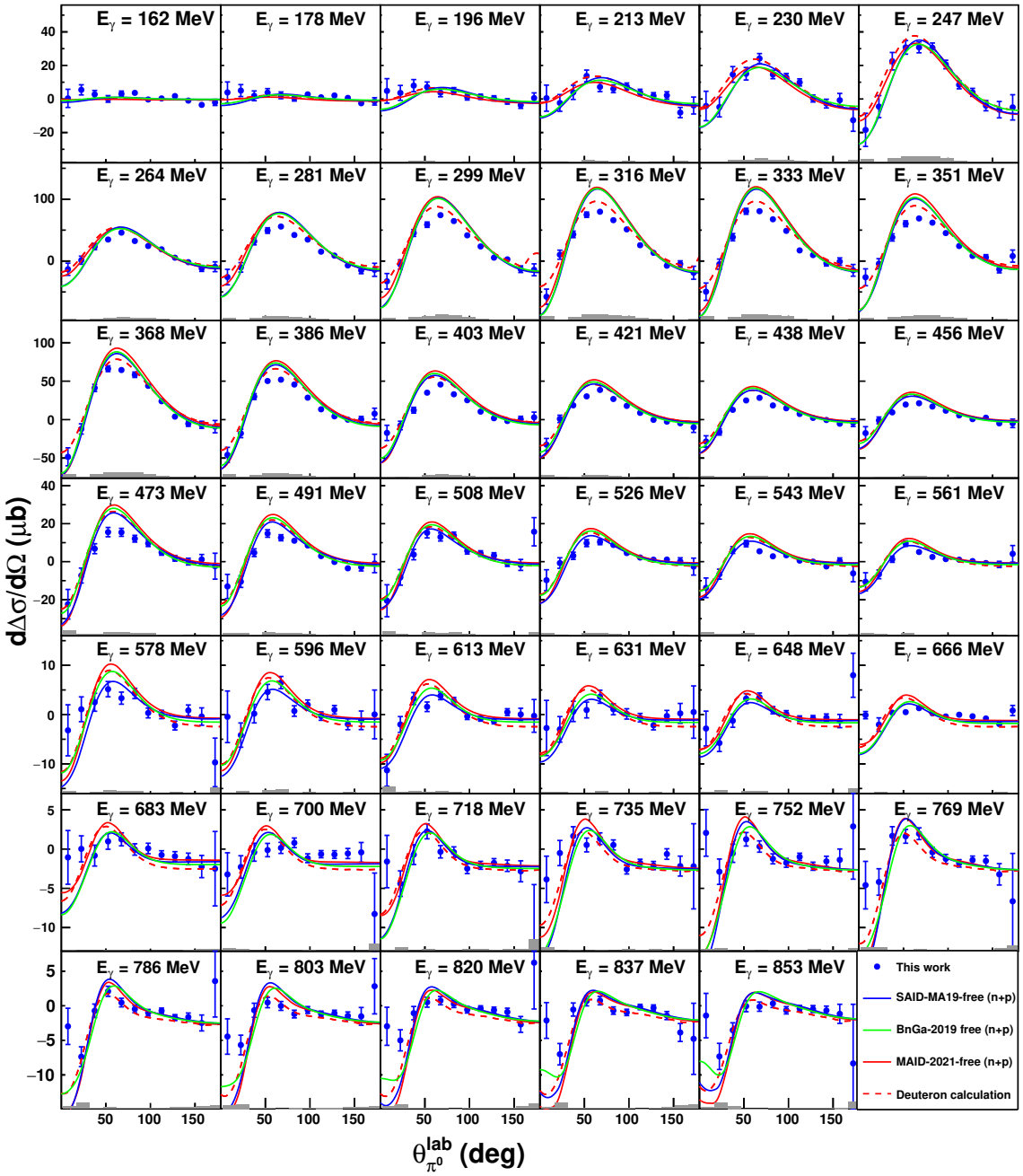

FIG. 12: Helicity-dependent differential cross section for single π^0 photoproduction on the deuteron as function of $\theta^{\rm LAB}_{\pi^0}$ for $E_\gamma < 860$ MeV. The color code for the theory curves is as in Fig. 11. The contributions of all the systematic uncertainties (see Sect. III F) are depicted as grey bars.

nuclear effects have little impact on this observable, at least under the quasi-free kinematic conditions. This fact is by no means trivial considering the strong influence of FSI, shown in Figs. 12 and 13. Thus, although the cross sections $\sigma^{\uparrow\downarrow/\uparrow\uparrow}$ themselves undergo a noticeable influence from the nuclear environment, this effect tends to almost completely cancel out in the ratio (Eq. 3). This feature is confirmed by the calculations on a deuteron (red dashed lines) which turn out to be very close to the free nucleon results over the major part of the energy range.

Discrepancies occur only in the low W bins and at very forward pion polar angles, for which, as the direct calculation

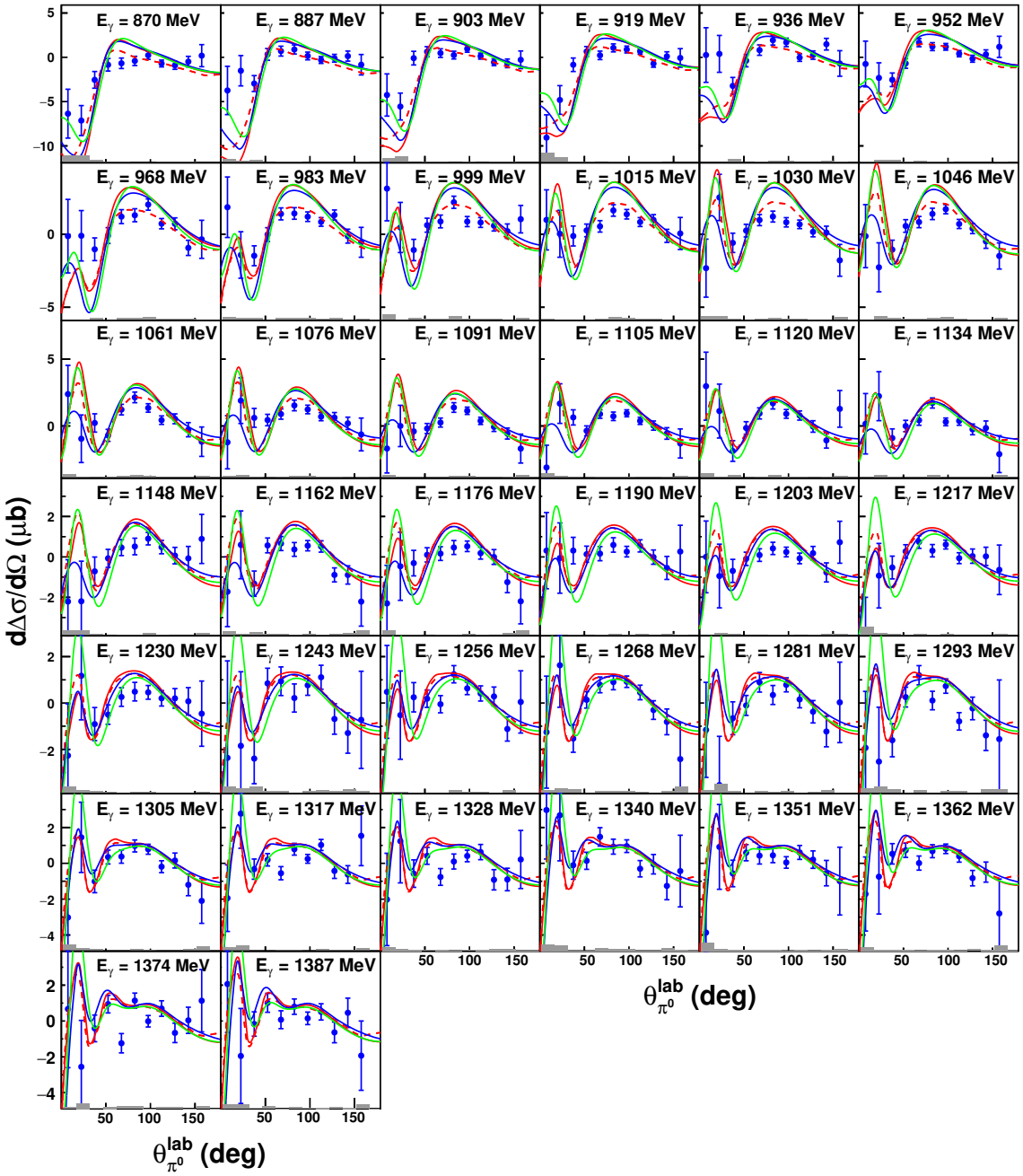

FIG. 13: Same as in Fig. 12 for $E_\gamma > 860$ MeV.

shows, the interaction between the final nucleons is mainly responsible. Namely, for W up to about 1300 MeV, the detection momentum threshold for nucleons ($p_N \gtrsim 350$ MeV/c) leads to a significant decrease of the phase-space available for quasi-free kinematics. As a result, a substantial fraction of the detected events comes from the kinematical region where the nuclear effects become relevant.

At the same time, as can be seen from the same figures, despite the rather low statistical accuracy in this W region, the model of Ref. [36] is able to reproduce the data quite well.

These new results are then particularly important for the neutron case. Since nuclear effects are basically isospin-independent, one can expect that photoproduction from bound neutrons in quasi-free kinematics can be used to extract the cross section on a free neutron, without the need to take into account different model-dependent corrections, at least above

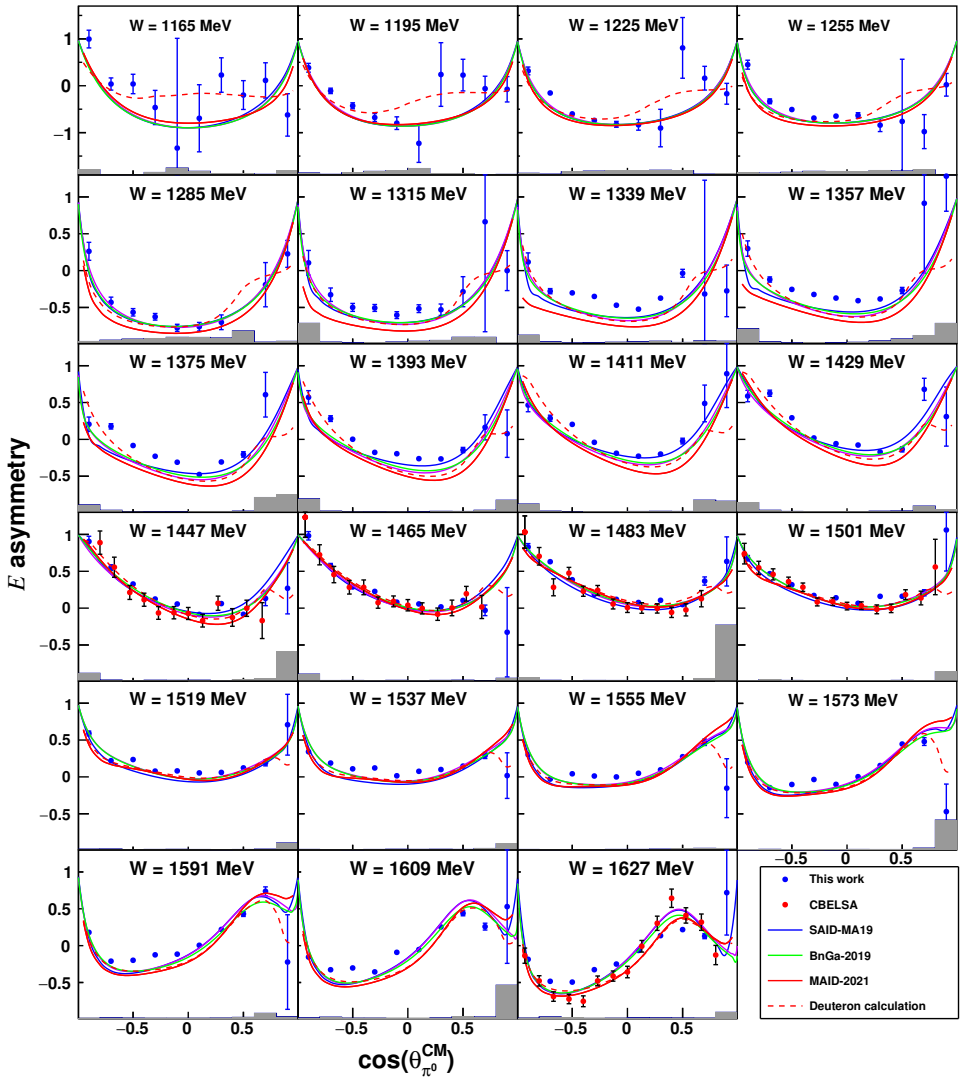

FIG. 14: Helicity asymmetry E for π^0 photoproduction on quasi-free protons as a function of $\cos(\theta)^{\rm CM}_{\pi^0}$ (blue points) in the energy range $W < 1627$ MeV. The pion angle $\theta^{\rm CM}_{\pi^0}$ refers to the $\pi^0 p$ center-of-mass frame. The new data are compared to the free proton results reported by CBELSA/TAPS collaboration [37, 38] as well as to the single nucleon calculation with SAID-MA19 [10], BnGa-2019 [33] and MAID-2021 [34] multipole amplitudes. The dashed lines show predictions for quasi-free protons obtained using the model of Ref. [35, 36] with the MAID-2021 amplitudes. The contributions of all the systematic uncertainties (see Sect. III F) are depicted as grey bars.

the first resonance region.

C. Double polarisation E observable for single π^0 on quasi-free neutron

The results of the double polarisation observable E for the single π^0 on quasi-free neutron are shown in Figs. 16 and 17, alongside with the theoretical predictions from the range of models described above. In this case, the present E data have been already included in the data base used to get the MAID-2021 predictions.

These are the first data on the angular distribution of the E observable on the neutron. The results for the angle-integrated E observable have already been published in Refs. [15, 30].

The nuclear model predictions show the same features of the proton case. This opens the possibility of obtaining access to the free-neutron information.

A quantitative evaluation of the impact of these new data on the existing multipole analyses can be obtained with the comparison of the predictions for the E observable on the neutron from fits made without and with their inclusion in the full data base. This comparison is shown in Fig. 18 using the MAID-2021 analysis. Using our new data a relevant change in the

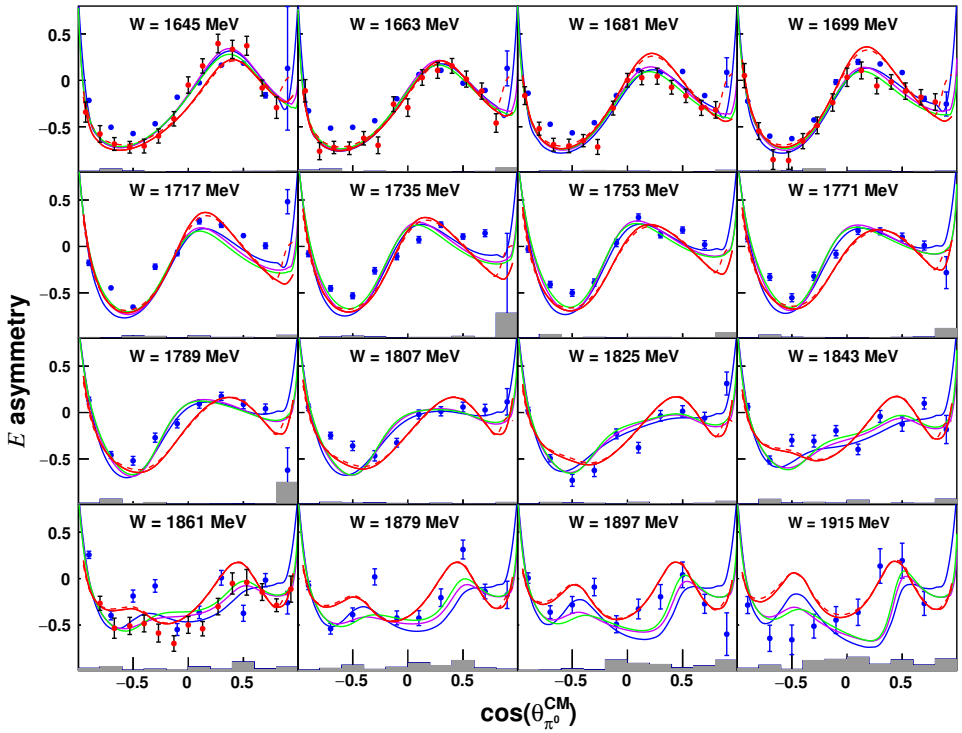

FIG. 15: Same as in Fig. 14 for quasi-free protons and $W > 1627$ MeV.

predictions can be noticed at about $W > 1650$ MeV.

At lower energies, where different data sets on different observables are available, the present data, as could reasonably be expected, do not significantly change the predictions given by the MAID-2021 partial wave analysis.

V. LEGENDRE FIT OF THE E DATA

To gain a better insight into the partial wave content of the reaction amplitude, one can also use expansion of the observables over Legendre polynomials. Such expansion can be very useful since the energy dependence of the expansion coefficients may reveal specific correlation between individual resonance states of definite parities (see, for instance,Ref. [39] and references therein).This method turns out to be especially effective in those cases when a single resonance (for example, $\Delta(1232)$) with well-known properties dominates in the amplitude in a certain energy range.

In the present paper, the Legendre coefficients a_k were obtained by fitting the angular distributions of the E asymmetry with a series of associated Legendre polynomials P_k:

$$\check{E}(W,\theta) = E(W,\theta)\cdot\frac{d\sigma_0}{d\Omega}(W,\theta) = \\ = \sum_{k=0}^{2l_{max}} (a_{l_{max}})_k(W) P_k(\cos\theta)\,. \qquad (10)$$

Here, the notation $(a_{lmax})_k$ means that in the fitting procedure only the partial waves with the πN relative angular momentum up to $l = l_{max}$ were included. The multipoles contributing to the fit for $l_{max} = 1,2,3$ are listed in Table II.

TABLE II: The multipole amplitudes contributing to the fitted cross section reported in Eq. (10) for different choices of l_{max}.

l_{max}	wave	M-poles
1	S-wave	E_{0^+}
	P-wave	$E_{1^+}, M_{1^+}, M_{1^-}$
2	D-wave	$E_{2^+}, E_{2^-}, M_{2^+}, M_{2^-}$
3	F-wave	$E_{3^+}, E_{3^-}, M_{3^+}, M_{3^-}$

For the unpolarised cross section $d\sigma_0/d\Omega$ in Eq. (10), we used the values given by the SAID-MA19 analysis. The latter are in good agreement with the available unpolarised data both on the proton and on the neutron. Replacing the SAID-MA19 analysis with the BnGa-2019 analysis gives almost the same results for a_k within statistical uncertainties.

The quality of our fit with $l_{max} = 1,2,3$ is demonstrated in Figs. 19 and 20 for several values of W. In the region $W < 1400$ MeV, where the $\Delta(1232)$ resonance dominates the angular dependence of $\check{E}$, it should be governed by the p-waves with relatively small admixture of the s-waves. The mallness of the s-wave part is explained by relative weakness of the electric dipole amplitude E_{0+}, which is responsible for production of the s-wave pions. In the π^0 channel, the s-wave is an order of magnitude smaller than the charged pion one. As

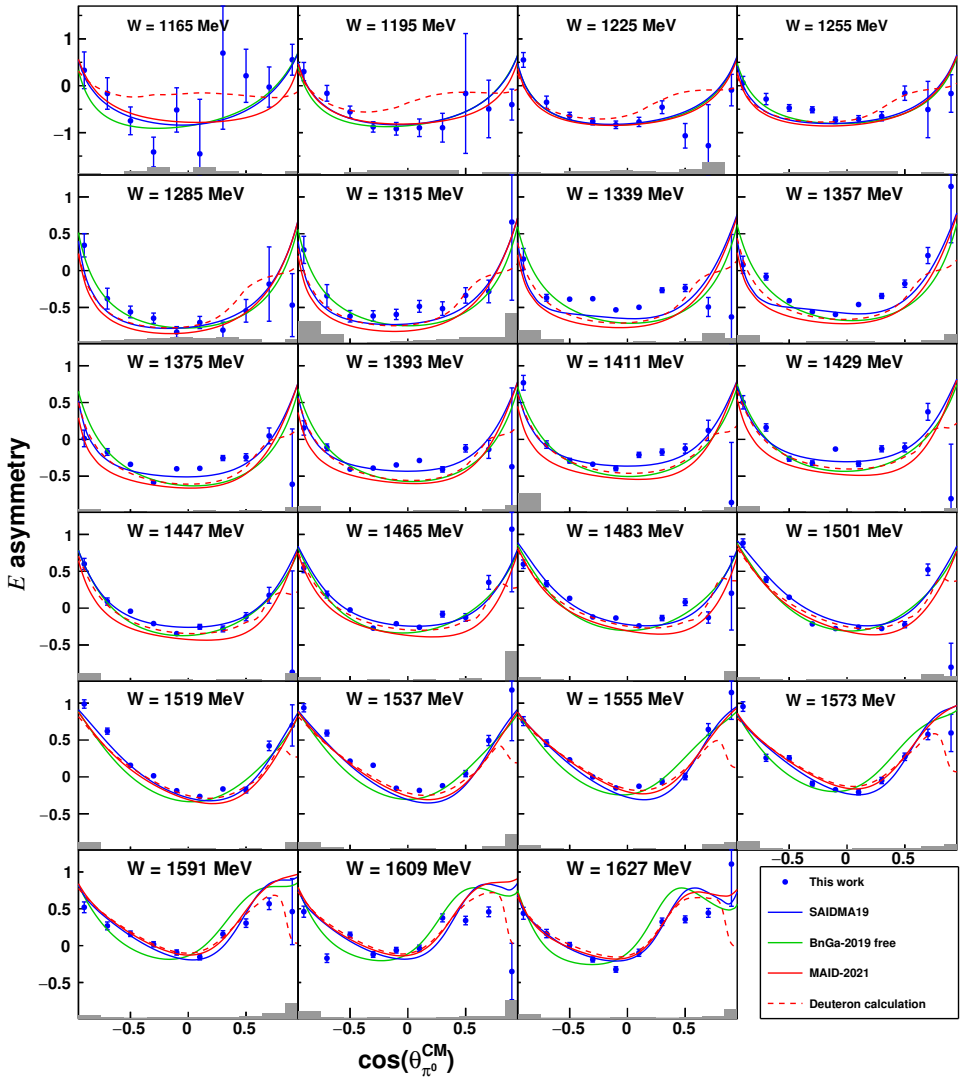

FIG. 16: Same as in Fig. 14 for quasi-free neutrons.

a result, in the wide energy range up to the second resonance region, the π^0 photoproduction proceeds almost exclusively via the magnetic dipole transition to the $\Delta(1232)$ resonance. There is also small admixture from the nucleon pole terms in the direct and the crossed channels from the magnetic γN coupling. Thus, taking $l_{max} = 1$ is expected to be sufficient to describe the general behavior of the data in a rather wide energy range. This thesis is fairly well supported by the experimental results in Figs. 19 and 20.

Above $W = 1400\,\text{MeV}$, the second resonance, $N(1520)$, starts to play a role, so that l needs to be expanded to $l_{max} = 2$ in order to take into account an increasing contribution of the D-waves.

Since the χ^2 value does not significantly change when going from $l_{max} = 2$ to $l_{max} = 3$ and only ten data points are available, $l_{max} = 2$ has been chosen as the best compromise between fit efficacy and our partial-wave analysis.

The investigation of the expansion given in Eq. (10)) reveals some important properties of the Legendre coefficients a_k. Firstly, parity conservation requires that the coefficients a_k with even k contain the products of multipoles $A_{l^\pm}A'_{l'^\pm}$ (with $A_{l^\pm} = E/M_{l^\pm}$) for which the difference $(l - l')$ takes only even values. Accordingly, the coefficients with odd k include products in which this difference is odd. This means that the odd coefficients are determined exclusively by the interference of the resonances with different parities. This property explains, in particular, the relative smallness of these coefficients in the entire energy range.

Another important property of the expansion coefficients is that the terms of the type $|E/M_{l^-}|^2$, quadratic in multipoles with total spin $j = l - 1/2$, contribute only to the coefficients a_0, ..., a_{2l-2} and do not appear in a_{2l}. This is obviously a consequence of the total angular momentum conservation. For this reason, for example, the coefficient a_4 does not contain

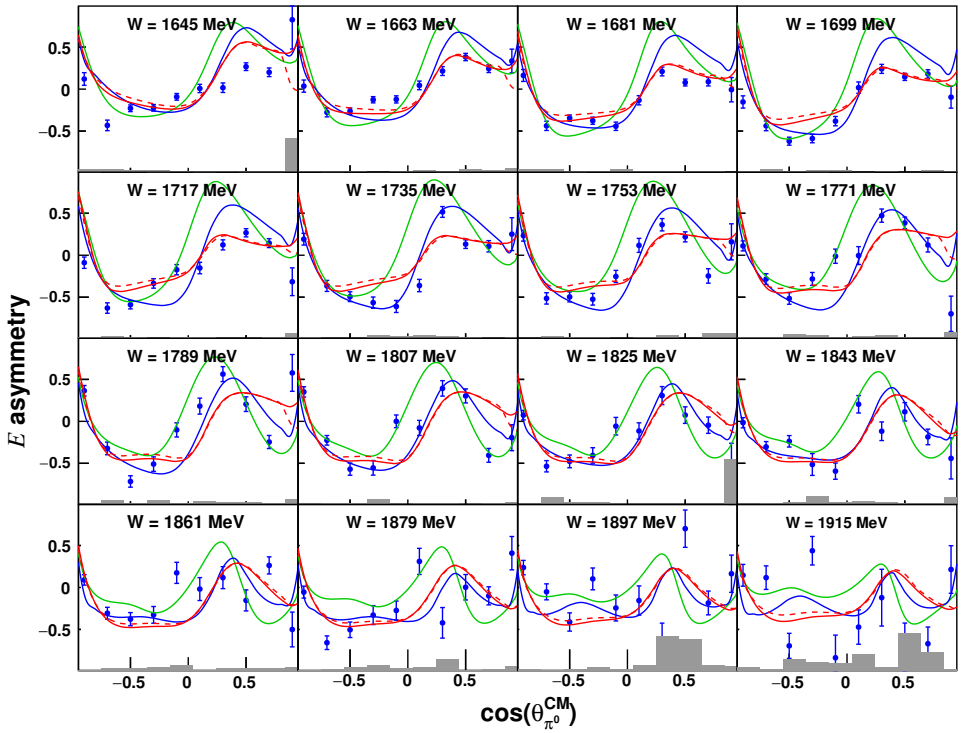

FIG. 17: Same as in Fig. 16 for quasi-free neutrons and $W > 1627$ MeV.

the terms $|E_{2^-}|^2$, $|M_{2^-}|^2$, and $E^*_{2^-}M_{2^-}$ of the resonance multipoles coming from $D_{13}(1520)$.

As follows from the discussion above, up to the energy $W \simeq 1400$ MeV the reaction is dominated by the p-wave multipole M_{1^+} due to the $\Delta(1232)$ excitation mechanism. A direct consequence of this dominance is a pronounced resonance to be expected in the coefficients a_0 and a_2 in the energy region around $W = 1230$ MeV, with all the remaining coefficients having very small values. This expected resonance behavior is observed. See inserts in $(a_2)_0$ and $(a_2)_2$ plots in Figs. 21 and 22.

The Legendre coefficients for the proton and the neutron channels given by the above described fit procedure are plotted in Fig. 21 and in Fig. 22, respectively, for $W > 1300$ MeV, a region where, as discussed before, nuclear effects are minimized and all the coefficient values are significantly different from zero.

In the insert plots of the fitted $(a_2)_0$ and $(a_2)_2$ coefficients, the only ones that have meaningful values in $\Delta(1232)$ resonance region, their values are given over the full measured W range. The curves represent the corresponding coefficients evaluated using the SAID-MA19 model.

It is interesting to note that the coefficient $(a_2)_0$ exhibits, as expected, a cusp structure at the η threshold ($W = 1487$ MeV) in both the $\pi^0 p$ and the $\pi^0 n$ channels. This effect, previously observed also for the $\Delta\sigma$ observable (see Fig. 11), is in particular due to interference of the negative parity state $S_{11}(1535)$ with the $\Delta(1232)$ resonance. For the same coefficient, the effect of the intermediate excitation of the $F_{15}(1680)$ resonance is clearly visible at higher energies in the proton case. This could be predicted from the much smaller absolute value of the $A_{3/2}$ helicity amplitude of this resonance in the neutron case.

As already discussed above, the $(a_2)_4$ coefficient does not contain the terms $A^*_{2^-}A'_{2^-}$, $A = E/M$, those determined by the D_{13} wave alone. In the case $l_{max} = 2$ its value is due only to the interference of the E/M_{2^-} and the E/M_{2^+} multipoles. The almost complete absence of the resonance-like structure around $W = 1500$ MeV is a trivial consequence of the smallness of the E/M_{2^+} amplitudes in this energy region.

The structure in the data at $W > 1600$ MeV, which is especially evident for the proton case, is due to the fact that our fit procedure is limited to $l_{max} = 2$. This artificially increases the contribution of the $D_{13}(1520)$ and $D_{15}(1650)$ to compensate the real effect due to the onset of $F_{15}(1680)$ resonance. As mentioned before, due to the limited number of angular bins and also to the limited statistical accuracy in the polar forward region, this contribution can not be properly evaluated.

In future, new experiments with higher statistics need then to be performed and also some residual contributions of the nuclear effects that, according to the deuteron calculation of Refs. [35, 36], are still present in the very forward polar region, also need to be carefully evaluated.

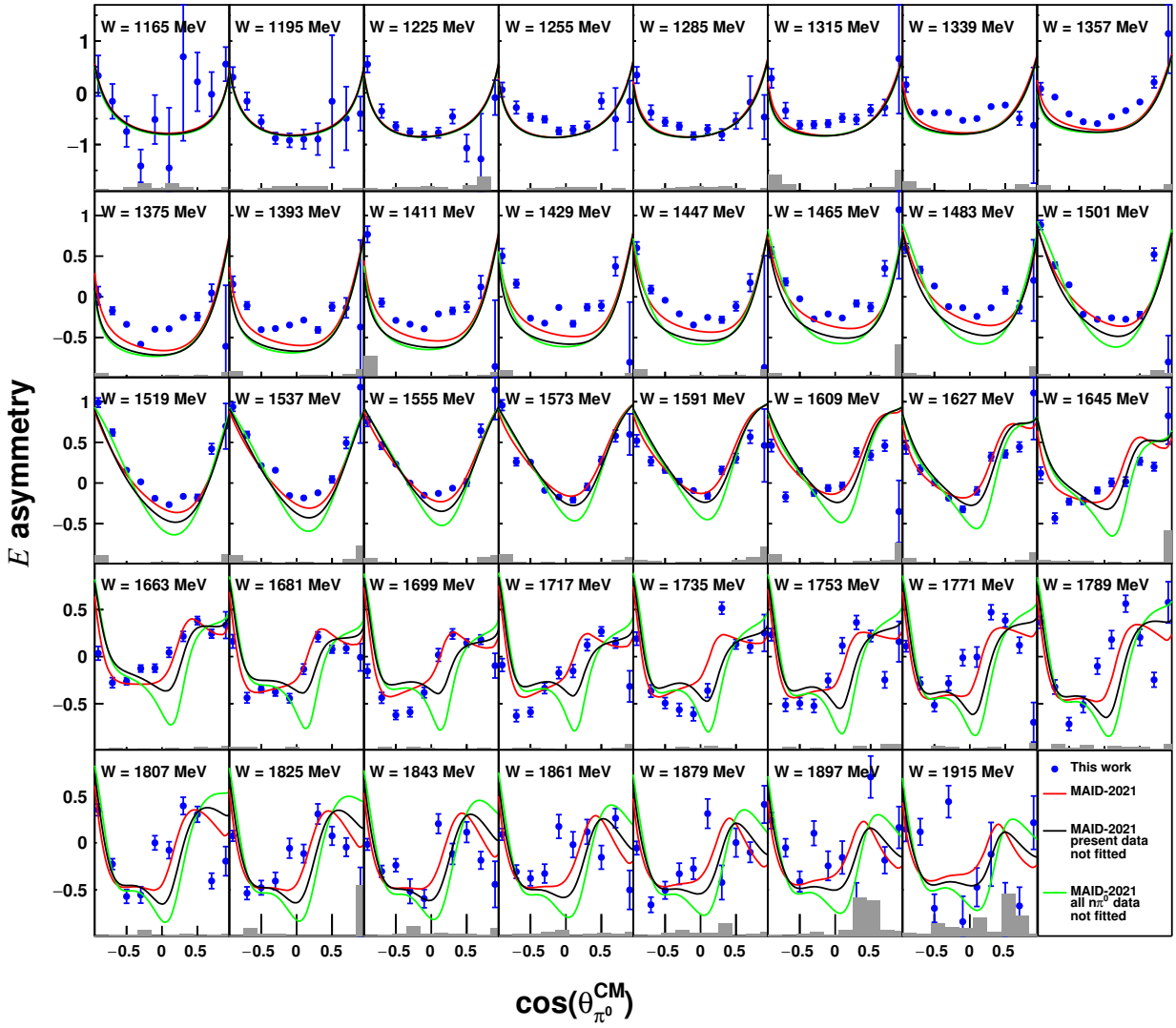

FIG. 18: MAID-2021 prediction for the helicity asymmetry E on the neutron from the fits made with (red line) and without (black line) including the present data into the fitted data base. The green line is the prediction obtained by excluding from the fit all the published $n\pi^0$ data.

VI. SUMMARY AND CONCLUSIONS

New precise data on the helicity-dependent inclusive cross section, as well as on the beam-target helicity spin asymmetry E of single π^0 photoproduction on the deuteron, have been obtained. Compared to existing data, the new measurements cover a wider energy range and have much better statistics.

Comparison with the free nucleon calculation allows the influence of nuclear effects on the single photoproduction mechanism to be evaluated quantitatively. This in turn gives valuable information about the extent to which these effects may distort the helicity asymmetry E, extracted from the quasi-free nucleon cross sections.

According to our results, the difference $d\Delta\sigma/d\Omega$ (see Eq. 9) of the helicity-dependent cross sections $\sigma^{\uparrow\downarrow/\uparrow\uparrow}$ exhibits rather different behaviors between free nucleons and nucleons inside deuterium.

At the same time, in the asymmetry E values measured for quasi-free nucleons, the nuclear effects are to a relevant extent canceled and can be disregarded almost in the whole energy range, except for energies below the $\Delta(1232)$ peak and, as also observed in Ref. [11] for the photon beam asymmetry, at the very forward pion angles. Therefore, these new data on E for quasi-free neutrons can be used to access this observable on the free neutrons without resorting to any model-dependent calculations.

A Legendre analysis of the new experimental results has already provided valuable information on the resonance states

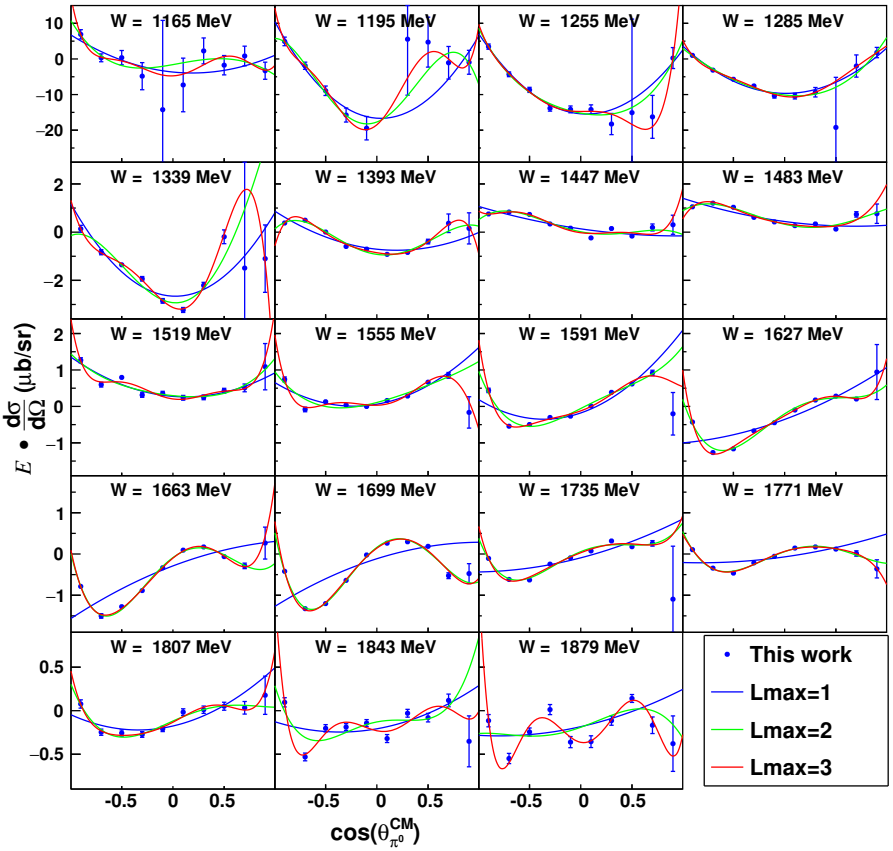

FIG. 19: The asymmetry $\check{E} = E\,d\sigma_0/d\Omega$ as function of $\cos(\theta)^{\rm CM}_{\pi^0}$ in the $\pi^0 p$ channel. Different fits are obtained with Legendre polynomial expansion given in Eq. (10) truncated at $l_{max} = 1$ (blue), 2 (green), and 3 (red).

contributing to the $\pi^0 n$ channel without performing a detailed partial wave analysis.

VII. ACKNOWLEDGMENTS

The authors wish to acknowledge the excellent support of the accelerator group of MAMI. This work has been supported by the U.K. STFC (ST/L00478X/1, ST/T002077/1, ST/L005824/1, 57071/1, 50727/1, ST/V001035/1) grants, the Deutsche Forschungsgemeinschaft (SFB443, SFB/TR16, and SFB1044), DFG-RFBR (Grant No. 09-02-91330), Schweizerischer Nationalfonds (Contracts No. 200020-175807, No. 200020-156983, No. 132799, No. 121781, No. 117601), the U.S. Department of Energy (Offices of Science and Nuclear Physics, Awards No. DE-SC0014323, DEFG02-99-ER41110, No. DE-FG02-88ER40415, No. DEFG02-01-ER41194) and National Science Foundation (Grants NSF OISE-1358175; PHY-1039130, PHY-1714833, No. IIA-1358175), INFN (Italy), and NSERC of Canada (Grant No. FRN-SAPPJ2015-00023). The calculation on the deuteron is supported by the Russian Science Foundation, grant No. 22-42-04401.

[1] I. Barker and A. Donnachie, Nucl. Phys. B 95 (1975) 347.
[2] G. Keaton and R. Workman, Phys. Rev. C 53 (1996) 1434.
[3] W. T. Chang and F. Tabakin, Phys. Rev. C 55 (1997) 2054.
[4] Y. Wunderlich, R. Beck and L. Tiator, Phys. Rev. C 89 (2014) 055203.
[5] Y. Wunderlich et al., Phys. Rev. C 102 (2020) 034605.
[6] W. Briscoe et al., Eur. Phys. J. A 58 (2022) 23.
[7] V. Tarasov *et al.*, Phys. Rev. C 84 (2016) 035203.
[8] V. Tarasov *et al.*, Phys. Atom. Nucl. 79 (2016) 216.
[9] P. Mattione *et al.*, (CLAS Collaboration), Phys. Rev. C 96 (2017) 035204.
[10] W. J. Briscoe *et al.* (A2 collaboration at MAMI), Phys. Rev. C 100 (2019) 065205.
[11] C. Mullen *et al.*, (A2 collaboration at MAMI), Eur. Phys. J. A 57 (2021) 205.

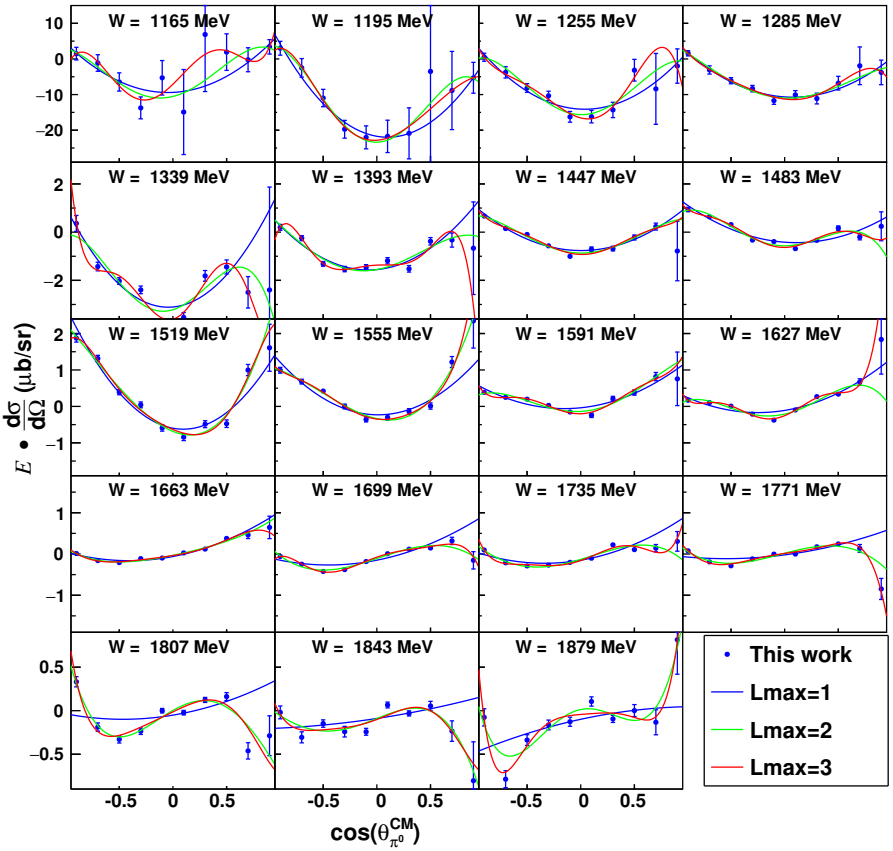

FIG. 20: Same as in Fig. 19 for the $\pi^0 n$ channel.

[12] A. Kaeser *et al.*, (A2 collaboration at MAMI), Eur. Phys. J. A 52 (2016) 272.
[13] M. Oberle *et al.*, Eur. Phys. J. A 50 (2014) 54.
[14] V. Sokhoyan *et al.*, (A2 collaboration at MAMI), Phys. Lett. B 802 (2020) 135243.
[15] M. Dieterle *et al.* (A2 Collaboration at MAMI), Phys. Lett. B 770 (2017) 523.
[16] E. Mornacchi, PhD thesis, University of Mainz, 2021.
[17] H. Kaiser *et al.*, Nucl. Instrum. Methods A 593 (2008) 159.
[18] L. Witthauer *et al.* (A2 collaboration at MAMI), Phys. Rev. C 95 (2017) 055201.
[19] M. Dieterle *et al.* (A2 collaboration at MAMI), Phys. Rev. C 97 (2018) 065205.
[20] J. C. McGeorge *et al.*, Eur. Phys. J. A 37 (2008) 129.
[21] H. Olsen and L. Maximon, Phys. Rev. 114 (1959) 887.
[22] C. Rohlof and H. Dutz, Nucl. Instrum. Methods A 436 (1999) 430.
[23] S. Goertz *et al.*, Nucl. Instrum. Methods A 526 (2004) 43.
[24] C. Bradtke *et al.*, Nucl. Instrum. Methods A 436 (1999) 430.
[25] A. Starostin *et al.*, Phys. Rev. C 64 (2001) 055205.
[26] R. Novotny *et al.*, IEEE Trans. Nucl. Sci. 38 (1991) 379.
[27] R. A. Gabler *et al.*, Nucl. Instrum. Methods A 346 (1994) 168.
[28] S. Agostinelli *et al.*, Nucl. Instrum. Methods A 506 (2003) 250.
[29] M. Dieterle *et al.* (A2 collaboration at MAMI), Eur. Phys. J. A 51 (2015) 142.
[30] M. Dieterle, PhD thesis, University of Basel, 2015.
[31] F. Cividini, PhD thesis, University of Mainz, 2020.
[32] J. Ahrens *et al.*, Phys. Lett. B 672 (2009) 328.
[33] A. V. Anisovich *et al.*, Eur. Phys. J. A 52 (2016) 284.
[34] V. Kashevarov and L. Tiator, 2021, Private communication.
[35] H. Arenhövel and A. Fix, Phys. Rev. C 72 (2005) 064004.
[36] A. Fix and H. Arenhövel, Phys. Rev. C 72 (2005) 064005.
[37] M. Gottschall *et al.* (CBELSA/TAPS Collaboration), Phys. Rev. Lett. 100 (2014) 012003.
[38] M. Gottschall *et al.* (CBELSA/TAPS Collaboration), Eur. Phys. J. A 57 (2021) 40.
[39] Y. Wunderlich et al., Eur. Phys. J. A 53 (2017) 86.

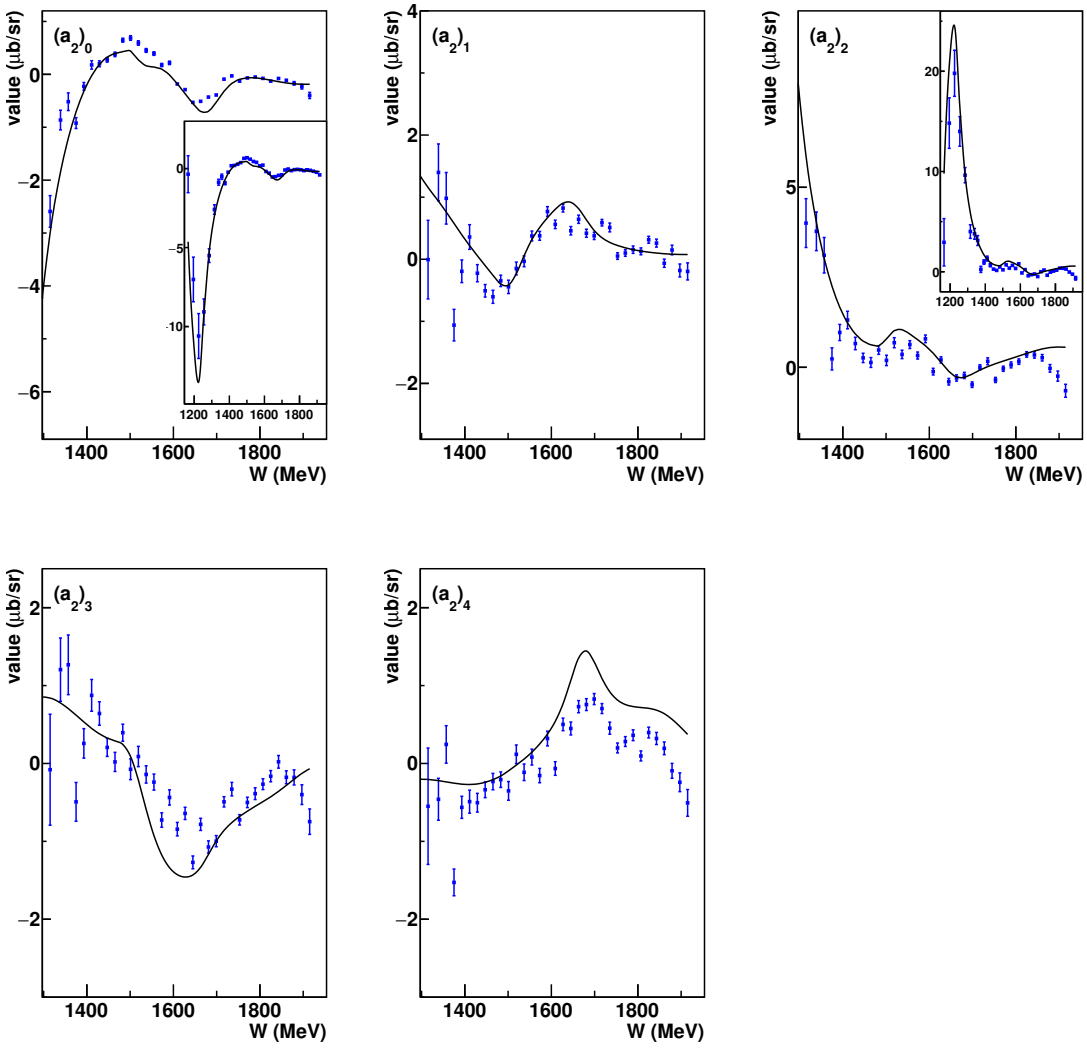

FIG. 21: Comparison of the fitted Legendre coefficients $(a_2)_k$ for the $\pi^0 p$ channel with the SAID-MA19 model predictions.

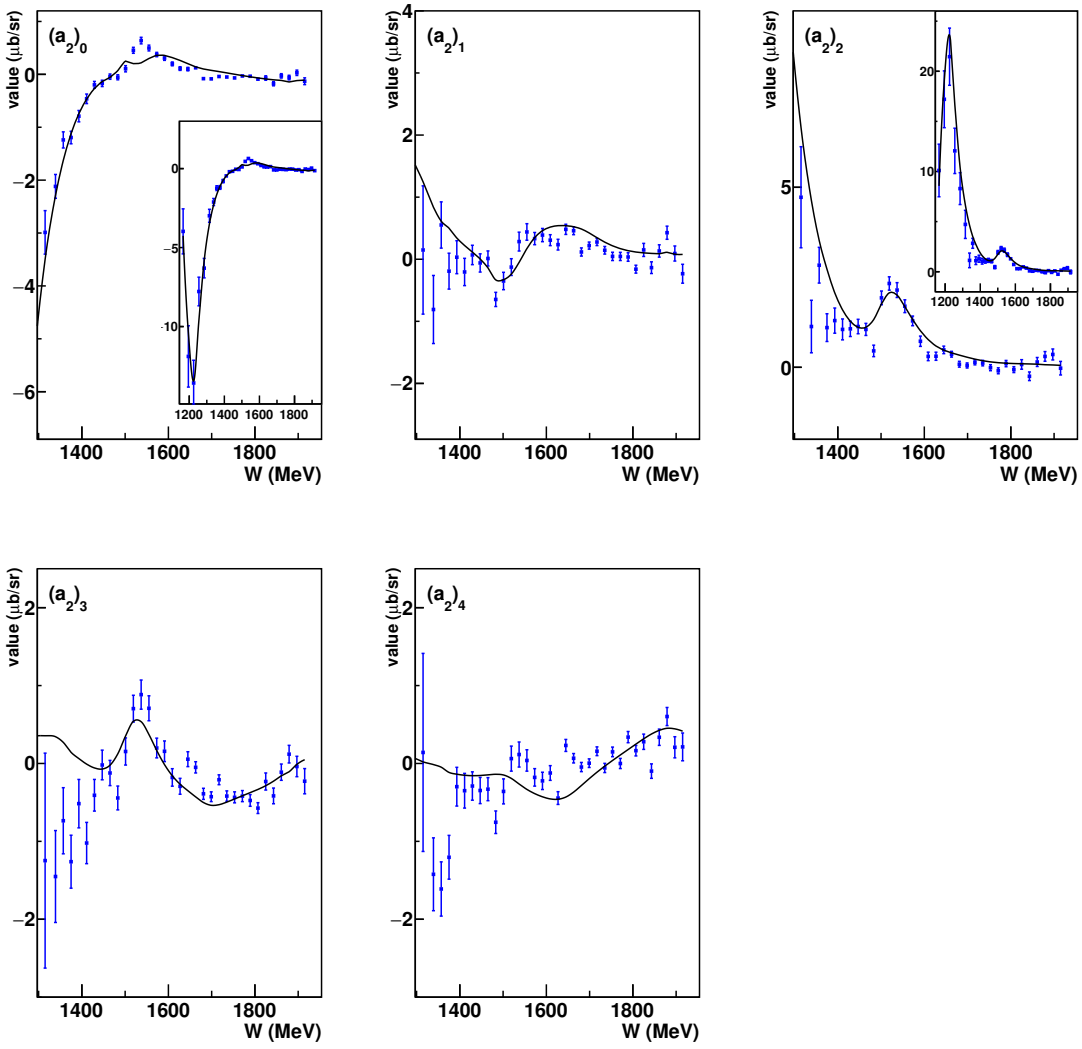

FIG. 22: Same as in Fig. 21 for the $\pi^0 n$ channel.